Model-Based Iterative Reconstruction for One-Sided Ultrasonic Non-Destructive Evaluation

Hani Almansouri[1], Singanallur Venkatakrishnan[2], Charles Bouman[1], and Hector Santos-Villalobos[2]

[1]Purdue University, 610 Purdue Mall, West Lafayette, IN 47907
[2]Oak Ridge National Laboratory, One Bethel Valley Road, Oak Ridge, TN 37831

***Abstract*—One-sided ultrasonic non-destructive evaluation (UNDE) is extensively used to characterize structures that need to be inspected and maintained from defects and flaws that could affect the performance of power plants, such as nuclear power plants. Most UNDE systems send acoustic pulses into the structure of interest, measure the received waveform and use an algorithm to reconstruct the quantity of interest. The most widely used algorithm in UNDE systems is the synthetic aperture focusing technique (SAFT) because it produces acceptable results in real time. A few regularized inversion techniques with linear models have been proposed which can improve on SAFT, but they tend to make simplifying assumptions that do not address how to obtain reconstructions from large real data sets. In this paper, we propose a model-based iterative reconstruction (MBIR) algorithm designed for scanning UNDE systems. To further reduce some of the artifacts in the results, we enhance the forward model to account for the transmitted beam profile, the occurrence of direct arrival signals, and the correlation between scans from adjacent regions. Next, we combine the forward model with a spatially variant prior model to account for the attenuation of deeper regions. We also present an algorithm to jointly reconstruct measurements from large data sets. Finally, using simulated and extensive experimental data, we show MBIR results and demonstrate how we can improve over SAFT as well as existing regularized inversion techniques.**

***Index Terms*—Non-Destructive Evaluation (NDE), Ultrasound imaging, Ultrasound Reconstruction, Model-Based Iterative Reconstruction (MBIR), Regularized Iterative Inverse, Synthetic Aperture Focusing Technique (SAFT).**

I. Introduction

One-sided ultrasonic non-destructive evaluation (UNDE) is widely used in many applications to characterize and detect flaws in materials, such as concrete structures in nuclear power plants (NPP), because of its low cost, high penetration, portability, and safety compared with other NDE methods [1]–[3]. A typical one-sided UNDE system consists of a sensor that transmits sound waves into the structures of interest and an array of receivers that measures the reflected signals (see Fig. 1). Such a set up is scanned across a large surface in a rectangular grid pattern and the reflected signals from each position are processed to reconstruct the underlying structure. The ability to easily probe structures that can only be accessed from a single side combined along with the ability of ultrasound signals to penetrate deep into structures make one-sided UNDE a powerful tool for the analysis of structures across a variety of applications [4], [5].

Reconstruction of structures from one-sided UNDE systems are challenging because of the complex interaction of ultrasound waves with matter, the geometry of the experimental set-up, the trade-off between resolution and penetration, and the potentially low signal-to-noise ratio of the received signals [6], [7]. The most widely used reconstruction method for UNDE is the synthetic aperture focusing technique (SAFT) [4], [8]–[12]. SAFT uses a delay-and-sum (DAS) approach to reconstruct ultrasound images. Fig. 2 shows an example of a SAFT reconstruction from real data. Notice that SAFT reconstructions tend to have significant artifacts due to the fact that SAFT assumes a simple propagation model and does not account for a variety of effects such as noise and image statistics, direct arrival signal artifacts, reverberation, and shadowing [11], [12]. In summary, while SAFT is computationally inexpensive to implement, it can result in significant artifacts in the one-sided UNDE reconstructions.

In order to overcome some of the short-comings of the SAFT method, regularized iterative reconstruction methods that use linear models (due to their low computational complexity) have recently been proposed for various ultrasound inverse problems. These methods formulate the reconstruction as minimizing a cost-function that balances a data fidelity term with a regularization applied to the image/volume to be reconstructed. The data fidelity term encodes a physics based model to reduce the error between the measurements and the projected reconstruction while the regularizer forces certain constraints on the reconstruction itself. For the data fidelity term, regularized iterative techniques for one-sided UNDE, such as [13], [14], use a simple linear model that models the propagation of the ultrasonic wave to reconstruct the reflectance B-mode images. A technique that uses the same forward model, but shows 2D images for a fixed depth (c-mode), is shown in [15]. The forward model in [15] has been upgraded to account for the beam profile as in [16] which can help in reducing some artifacts. However, this forward model does not account for direct arrival signals

This manuscript has been authored by UT-Battelle, LLC under Contract No. DE-AC05-00OR22725 with the U.S. Department of Energy. The United States Government retains and the publisher, by accepting the article for publication, acknowledges that the United States Government retains a non-exclusive, paid-up, irrevocable, world-wide license to publish or reproduce the published form of this manuscript, or allow others to do so, for United States Government purposes. The Department of Energy will provide public access to these results of federally sponsored research in accordance with the DOE Public Access Plan (http://energy.gov/downloads/doe-public-access-plan).

caused by coupling the ultrasonic device to the surface of the structure which might cause artifacts and interference with reflections. Furthermore, the reconstruction algorithm of [16] is not designed to exploit correlations between adjacent scans for systems with large field-of-view.

In [14], [16]–[18], the authors used a simple regularization terms, such as l_1 or l_2. This regularization is suitable for imaging point scatters or sparse regions. However, for more complex medium where edge preservation is needed, other techniques use a more sophisticated regularization, such as total variation, where they showed significant enhancement over SAFT [13], [15]. The method in [13] uses total variation with variety of a regularization terms that are depth dependent to resolve the attenuation and blurring for deeper reflections. However, the depth-dependent regularization is linear with depth which might not be the best modeling for the depth attenuation. Therefore, while regularized inversion methods that use a linear forward model have shown promise in certain applications, they do not deal with the direct arrival signal artifacts in a principled manner, they have not been designed to jointly handle large data sets that require multiple scanning for one-sided UNDE systems, and they do not fully account for the depth-dependent blurring that can occur by the use of certain regularizers.

In this paper, we propose an ultrasonic model-based iterative reconstruction (MBIR) algorithm designed specifically for one-sided UNDE systems of large structures. We resolve the issues discussed above by enhancing the forward and prior models used in the current regularized iterative techniques. The enhancement to the forward model include a direct arrival signal model with varying acoustic speed and an anisotropic modeling of the transmitted signal propagation to reduce some of the artifacts in the reconstruction. Also, we repopulate the system matrix of the forward model to generate a larger system matrix for larger field of views to share more information about adjacent scans which can help in reducing noise and artifacts and enhancing the reconstruction. Furthermore, the prior model is enhanced by increasing and conveniently controlling the regularization for deeper regions to reduce the attenuation to these regions. In previous work, we have demonstrated the performance of MBIR compared with SAFT using different combinations of these enhancements [19]–[21]. We introduce four major contributions in this paper:

1) A physics-based linear forward model that models the direct arrival signal with varying acoustic speed, absorption attenuation, and anisotropic propagation;
2) A non-linear spatially-variant regularization to enhance the reconstruction for deeper regions;
3) A systematic way using joint-MAP stitching and 2.5D MBIR to reconstruct the volume from all the measured data simultaneously rather than individual reconstruction;
4) Qualitative and quantitative results from simulated and extensive experimental data.

The paper is organized as follows. In section II we cover the design for the forward model of the ultrasonic MBIR for one-sided NDE applications. In section III we cover the prior model used for MBIR. In section IV we cover the optimization of the MAP cost function using the ICD method. In section V we cover simulated and experimental results from MBIR and other techniques. In section VI we cover the conclusion.

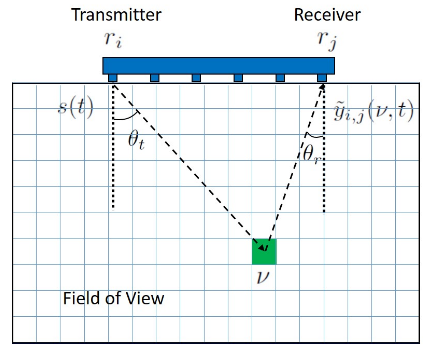

Fig. 1. An illustration of a typical one-sided UNDE problem where $s(t)$ is the transmitted signal, ν is a point in the field-of-view, $y_{i,j}(\nu, t)$ is the received signal reflected from ν, θ_t is the angle between r_i and ν, and θ_r is the angle between r_j and ν.

II. Forward Model of One-Sided UNDE

The reconstruction in an MBIR setting is given by the following minimization problem,

$$x_{MAP} = \underset{(x)}{\arg\min} \left\{ -\log p(y|x) - \log p(x) \right\},$$

where x is the image to be reconstructed, y is the measured data, x_{MAP} is the reconstructed image, $p(y|x)$ is the forward model and the probability distribution of y given x, $p(x)$ is the prior model and the probability distribution of x. The forward model is designed in the following way. We will consider a one-sided UNDE for a concrete structure where the transducers are coupled to the surface as shown in Fig. 1. We will consider a pressure signal (Pascal) transmitted from transducer i located at position $r_i \in \mathbb{R}^3$, reflected by a point located at $\nu \in \mathbb{R}^3$, and received by transducer j located at $r_j \in \mathbb{R}^3$. We assume the Fourier transform of the temporal impulse response of a system sending a signal from r_i and receiving from ν to be

$$G(r_i, \nu, f) = \lambda e^{-(\alpha(f)+j\beta(f))\|\nu - r_i\|}$$

where λ is a transmittance coefficient,

$$\alpha(f) = \alpha_0 |f| \qquad (\mathrm{m}^{-1})$$

is the rate of attenuation,

$$\beta(f) = \frac{2\pi f}{c} \qquad (\mathrm{m}^{-1})$$

is the phase delay due to propagation through the specimen, and c is the speed of sound [22]–[28]. Similarly, we assume the Fourier transform of the impulse response of a system sending a signal from ν and receiving from r_j to be

$$G(\nu, r_j, f) = \lambda e^{-(\alpha(f)+j\beta(f))\|r_j - \nu\|} .$$

Assuming $s(t)$ (Pascal) is the input to the system and $\tilde{x}(\nu)$ (m^{-3}) is the reflectivity coefficient for ν, then the output $\tilde{Y}_{i,j}(\nu, f)$ (Pascal $\cdot\, \mathrm{m}^{-3} \cdot \mathrm{Hz}^{-1}$) at the receiver due to ν is

$$\begin{aligned}\tilde{Y}_{i,j}(\nu, f) &= -S(f)G(r_i, \nu, f)\tilde{x}(\nu)G(\nu, r_j, f)\\ &= -\lambda^2 \tilde{x}(\nu) S(f) e^{-(\alpha_0 c|f| + j2\pi f)\tau_{i,j}(\nu)},\end{aligned}$$

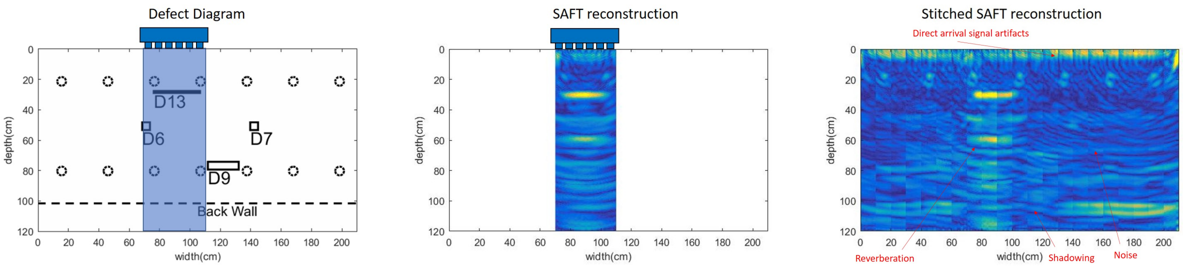

(a) (b) (c)

Fig. 2. Example of a SAFT reconstruction from real data of a concrete structure. (a) shows the defect diagram containing steel rebars (dotted circles), defects (marked D#), and the back wall (dotted line). (b) shows SAFT reconstruction for a single scan of the large field-of-view in (a). (c) shows the SAFT reconstruction for the entire field-of-view after stitching the results from each individual scan.

where

$$\tau_{i,j}(\nu) \quad = \quad \frac{\|\nu - r_i\| + \|\nu - r_j\|}{c} \qquad (\mathrm{s}).$$

By defining

$$\tilde{h}(\tau_{i,j}(\nu), t) = \mathcal{F}^{-1}\left\{-\lambda^2 S(f) e^{-\alpha_0 c|f|\tau_{i,j}(\nu)}\right\}, \tag{1}$$

where $\mathcal{F}^{-1}$ is the inverse Fourier transform, the time domain output signal, $\tilde{y}_{i,j}(\nu, t)$ (Pascal $\cdot\, \mathrm{m}^{-3}$), is given by

$$\tilde{y}_{i,j}(\nu, t) = \tilde{h}(\tau_{i,j}(\nu), t - \tau_{i,j}(\nu))\, \tilde{x}(\nu).$$

Note that $\tilde{h}(\tau_{i,j}(\nu), t)$ is a function of $\tau_{i,j}$ and t, i.e. not directly a function of ν. This is a very useful property that can reduce the computational cost of evaluating $\tilde{h}$. In many cases, $\tilde{h}(\tau, t)$ for any τ is close to zero after a certain time t_0. In this case, it is very helpful to modify the previous equation to

$$\tilde{y}_{i,j}(\nu, t) = h(\tau_{i,j}(\nu), t - \tau_{i,j}(\nu))\, \tilde{x}(\nu).$$

where

$$\begin{aligned} h(\tau, t) \quad &= \quad \tilde{h}(\tau, t) \ \mathrm{rect}\left(\frac{t}{t_0} - \frac{1}{2}\right), \\ \mathrm{rect}(x) \quad &= \quad 1 \text{ for } |x| < \frac{1}{2} \text{ and } 0 \text{ for } |x| \geq \frac{1}{2}, \end{aligned}$$

and t_0 is a constant where we assume $h(\tau, t)$ is equal to zero for $t > t_0$. Applying the rect function is very helpful in increasing the sparsity of the system matrix which leads to a dramatic decrease in memory and processing time. To get the overall output $\tilde{y}_{i,j}(t)$ (Pascal) from all points in $\mathbb{R}^3$, we need to integrate over all ν:

$$\begin{aligned} \tilde{y}_{i,j}(t) \quad &= \quad \int_{\mathbb{R}^3} \tilde{y}_{i,j}(\nu, t) d\nu & (2) \\ &= \quad \int_{\mathbb{R}^3} \tilde{A}_{i,j}(\tau_{i,j}(\nu), t) \tilde{x}(\nu) d\nu\ , & (3) \end{aligned}$$

where

$$\tilde{A}_{i,j}(\tau_{i,j}(\nu), t) = h(\tau_{i,j}(\nu), t - \tau_{i,j}(\nu)). \tag{4}$$

For simplicity, the set of all transducer pairs, $\{i, j\}$, is mapped to the ordered set $\{1, ..., K\}$, where K is the total number of transducer pairs. Hence, Eq. 3 becomes

$$\tilde{y}_k(t) = \int_{\mathbb{R}^3} \tilde{A}_k(\tau_k(\nu), t) \tilde{x}(\nu) d\nu\ . \tag{5}$$

Finally, we assume the noise associated with the measurements to be i.i.d. Gaussian.

A. *Direct Arrival Signal Artifacts*

When the ultrasonic device is attached or coupled to the surface of the concrete, a direct arrival signal is generated along with the transmitted signal. This direct arrival signal produces artifacts on the reconstructed image in regions closer to the transducer and it might interfere with some of the reflected signals (see Fig. 2). Eq. 5 models the output from the reflection of all points. However, the equation does not account for the direct arrival signal. Locating and deleting the direct arrival signal from the received signal eliminates the artifacts, but might lead to deleting reflection signals for closer objects. We propose a modification to the forward model that models the direct arrival signal and attenuates the artifact while preserving information from reflected signals. The modification adds the following term to the forward model in Eq. 5 that corresponds to the direct arrival signal,

$$\tilde{y}_k(t) = \int_{\mathbb{R}^3} \tilde{A}_k(\tau_k(\nu), t) \tilde{x}(\nu) d\nu + \tilde{d}_k(t)\ g_k, \tag{6}$$

where $\tilde{d}_k(t)$ is an additional term used to model the direct arrival signal given by

$$\begin{aligned} \tilde{d}_k(t) \quad &= \quad -\tilde{A}_k(\tau_k, t), \\ \tau_k \quad &= \quad \frac{\|r_i - r_j\|}{c}, \end{aligned}$$

and g_k is an unknown scaling coefficient for the direct arrival signal.

The above model works efficiently when the acoustic speed is constant. For a non-homogeneous material, such as concrete, the acoustic speed is not constant. This change in acoustic speed changes the location of the direct arrival signal and causes a mismatch with MBIR's direct arrival signal modeling. We can estimate the shift error by searching for the delay that produces the maximum autocorrelation of the direct arrival signal,

$$\begin{aligned} \hat{l} \quad &= \quad \underset{-\bar{\tau} \leq l \leq \bar{\tau}}{\arg\max} \left\{ \int \tilde{y}_k(t) \tilde{d}_k(t - l) dt \right\} \\ \tilde{d}_k(t) \quad &\leftarrow \quad \tilde{d}_k(t - \hat{l}), \end{aligned}$$

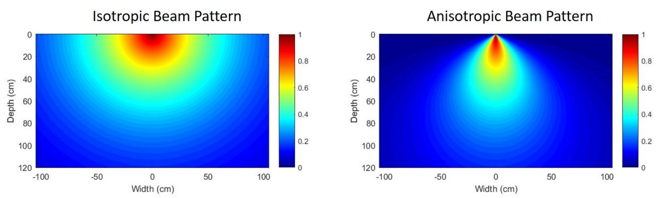

Fig. 3. Beam pattern model for an ultrasound transducer placed at (0,0) for isotropic propagation (left) and anisotropic propagation (right). Left image shows equal propagation in all direction. Right image shows more attenuation as the angle between the transmitter and the pixel increases.

where $\tilde{\tau}$ is chosen to be small, e.g. 3 sampling periods, to insure the shift is within the integral boundaries and to avoid interfering with later reflections. This estimate finds the shift error with the assumption that reflections do not interfere with the direct arrival signal. Therefore, for homogeneous medium, our approach is able to reduce direct arrival signal artifacts and detect reflections close to the transducers. However, for non-homogonous medium, our approach is able to reduce direct arrival signal artifacts that do not interfere with reflections.

B. Anisotropic Propagation

Many models used in UNDE assume that the profile of the transmitted beam is isotropic [15], [29]. However, this assumption is not valid for many systems and it can produce artifacts. While it would be ideal to know the precise profile especially of the transmitted beam, in systems that we deal with, this is not known. Therefore, we adopt a similar apodization function as in [4] for the anisotropic model. However, the apodization function used in [4] has a slow attenuating window. In our application, a faster attenuating window is needed. We use an anisotropic beam pattern model as shown in Fig. 3. We define a function, $\phi_k(\nu)$, that has a value ranging from 0 to 1. This function depends on the angles from the transmitter to ν and from ν to the receiver. $\phi_k(\nu)$ is monotonically decreasing with respect to those two angles. $\phi_k(\nu)$ can act as an attenuating window, such as cosine or Gaussian windows, to the output. The function $\phi_k(\nu)$ is added to Eq. 4 as follows:

$$\tilde{A}_k(\tau_k(\nu), t) = h(\tau_k(\nu), t - \tau_k(\nu))\phi_k(\nu). \tag{7}$$

Note that the beam pattern is assumed to be reciprocal, i.e. the receiver will also have the same beam pattern. In this paper, we chose $\phi_k(\nu)$ to be

$$\phi_k(\nu) = \cos^2(\theta_t(\nu))\cos^2(\theta_r(\nu)) \quad ,$$

where θ_t is the angle between the transmitter and ν and θ_r is the angle between the receiver and ν shown in Fig. 1.

Finally, the discretized version of the forward model can be used in the MAP estimate as shown below,

$$-\log p(y|x) = \frac{1}{2\sigma^2}\|y - Ax - Dg\|^2 + \text{constant},$$

where $y \in \mathbb{R}^{MK\times 1}$ is the measurement, σ^2 is the variance of the measurement, $A \in \mathbb{R}^{MK\times N}$ is the forward model (system matrix), $x \in \mathbb{R}^{N\times 1}$ is the image, $D \in \mathbb{R}^{MK\times K}$ is the direct arrival signal modeling matrix, $g \in \mathbb{R}^{K\times 1}$ is a vector containing scaling coefficients for the direct arrival signals, M is the number of measurement samples, and N is the number of pixels. The columns of D, d_k, are the discretized version of $\tilde{d}_k$. The vector g is used to scale each column of D independently.

C. Joint-MAP Stitching

In order to scan large regions, the sensor assembly is typically moved from one region to another on the surface in raster order to build up a 3D profile of the structure. Typically each data set is individually processed and placed together to present the overall 3D reconstruction, Fig. 4. However, this method results in sharp discontinuities at the boundaries and inefficient use of the data collected, Fig. 2. We design a joint-MAP technique to solve these issues by modifying the forward model to perform the stitching internally as part of the estimation. This technique is able to remove all discontinuities between the sections, make use of any additional information from adjacent scans, and process each pixel in the large field-of-view once. Furthermore, the system matrix used in the proposed joint-MAP technique is designed to arrange the small system matrices of single scans in an efficient way to increase the sparsity and reduce the required memory without requiring additional processing time for the reconstruction. We assume that adjacent scans share some columns of pixels and has some useful correlation that needs to be exploited to produce better images. Therefore, the forward model will account for those shared columns differently than the rest of the pixels or columns. For L measurements, we let the system matrix for each measurement be A and the image for each measurement be x_l. We let the order of the pixels in x_l be from top to bottom for each column starting from the far left column to the far right column. Hence, the term associated with the modified forward model in the MAP estimate will be

$$\frac{1}{2\sigma^2}\left\| y_{JMAP} - A_{JMAP}x_{JMAP} - D_{JMAP}g_{JMAP} \right\|^2, \tag{8}$$

where

$$A_{JMAP} = \begin{bmatrix} [\quad A &]\ 0 & 0 & \dots \\ 0 & [\quad A &]\ 0 & \dots \\ 0 & 0 & [\quad A \quad] & \dots \\ \vdots & \vdots & \vdots & \ddots \end{bmatrix},$$

$$D_{JMAP} = \begin{bmatrix} D & 0 & \dots & 0 \\ 0 & D & \dots & 0 \\ \vdots & \vdots & \ddots & \vdots \\ 0 & 0 & \dots & D \end{bmatrix},$$

$$y_{JMAP} = \begin{bmatrix} y_1 \\ \vdots \\ y_l \\ \vdots \\ y_L \end{bmatrix}, \quad g_{JMAP} = \begin{bmatrix} g_1 \\ \vdots \\ g_l \\ \vdots \\ g_L \end{bmatrix},$$

and x_{JMAP} is the image of the large field-of-view. A_{JMAP} is designed so that if a pixel is shared in more than one image,

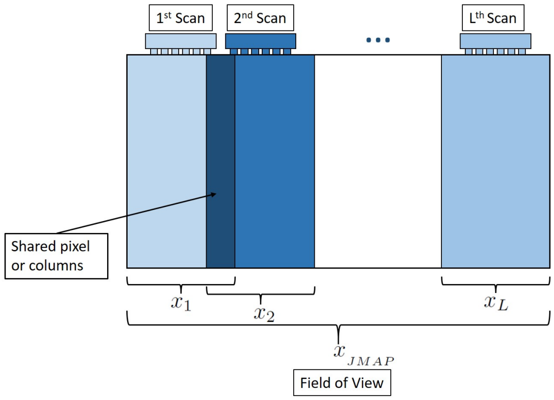

Fig. 4. An illustration of multiple measurements needed to scan a large field-of-view. Images from each scan share some pixels with its neighbor images. Proper stitching technique is needed to account for this shared areas in the field-of-view.

then its corresponding column in the system matrix for one image will be aligned with its corresponding columns in the system matrix for other images. For the example shown in Fig. 4, we can accomplish this alignment by shifting each system matrix A left or right until the required alignment is achieved.

III. Prior Model Of The Image

We design the prior model of the image to be a combination of a Gibbs distribution and an exponential distribution, i.e.

$$-\log p(x) = \sum_{\{s,r\}\in C} b_{s,r}\ \rho(x_s - x_r, \sigma_g) + \sum_{s\in S} \frac{x_s}{\sigma_e} + \text{constant},$$

where C is the set of all pair-wise cliques, S is the set of all pixels in the field of view, $b_{s,r}$ is a scaling coefficient, ρ is the potential function, σ_g is the regularization constant for the Gibbs distribution, σ_e is the regularization constants for the exponential distribution, and $x_s \geq 0\ \forall s \in S$. We chose the q-generalized Gaussian Markov random field (QGGMRF) as the potential function for the Gibbs distribution [30]. The equation for the QGGMRF is

$$\rho(\Delta, \sigma_g) = \frac{|\Delta|^p}{p\sigma_g^p}\left(\frac{|\frac{\Delta}{T\sigma_g}|^{q-p}}{1+|\frac{\Delta}{T\sigma_g}|^{q-p}}\right), \tag{9}$$

where $1 \leq p < q = 2$ insures convexity and continuity of first and second derivatives, and T controls the edge threshold. The Gibbs distribution is used to preserve edges while the exponential distribution is used to force the background toward zero.

The neighbors of a pixel s are arranged as

$$\begin{bmatrix} r_1 & r_2 & r_3 \\ r_4 & r_5 & r_6 \\ r_7 & r_8 & r_9 \end{bmatrix}, \begin{bmatrix} r_{10} & r_{11} & r_{12} \\ r_{13} & s & r_{14} \\ r_{15} & r_{16} & r_{17} \end{bmatrix}, \begin{bmatrix} r_{18} & r_{19} & r_{20} \\ r_{21} & r_{22} & r_{23} \\ r_{24} & r_{25} & r_{26} \end{bmatrix}. \tag{10}$$

where the neighbors with index 10 to 17 are from the same layer, and the rest of the neighbors are from the next and previous layers. With this arrangement, the scaling coefficients $b_{s,r}$ are chosen to be

$$\begin{aligned}
\begin{bmatrix} b_{s,r_1} & b_{s,r_2} & b_{s,r_3} \\ b_{s,r_4} & b_{s,r_5} & b_{s,r_6} \\ b_{s,r_7} & b_{s,r_8} & b_{s,r_9} \end{bmatrix} &= \begin{bmatrix} 0 & 0 & 0 \\ 0 & 2 & 0 \\ 0 & 0 & 0 \end{bmatrix} \cdot \frac{\gamma}{4\gamma+12}, \\
\begin{bmatrix} b_{s,r_{10}} & b_{s,r_{11}} & b_{s,r_{12}} \\ b_{s,r_{13}} & 0 & b_{s,r_{14}} \\ b_{s,r_{15}} & b_{s,r_{16}} & b_{s,r_{17}} \end{bmatrix} &= \begin{bmatrix} 1 & 2 & 1 \\ 2 & 0 & 2 \\ 1 & 2 & 1 \end{bmatrix} \cdot \frac{1}{4\gamma+12}, \\
\begin{bmatrix} b_{s,r_{18}} & b_{s,r_{19}} & b_{s,r_{20}} \\ b_{s,r_{21}} & b_{s,r_{22}} & b_{s,r_{23}} \\ b_{s,r_{24}} & b_{s,r_{25}} & b_{s,r_{26}} \end{bmatrix} &= \begin{bmatrix} 0 & 0 & 0 \\ 0 & 2 & 0 \\ 0 & 0 & 0 \end{bmatrix} \cdot \frac{\gamma}{4\gamma+12},
\end{aligned}$$

with a free boundary condition. The parameter γ is set to zero when 2D MBIR is needed, or greater than zero when a 3D regularization (2.5D MBIR) is needed. 2.5D MBIR can be used to gain more information from neighbors of different layers to reduce noise and increase resolution.

A. Non-linear Spatially-Variant Regularization

The standard form of the regularization introduced above uses constant σ_g and σ_e for all voxels. However, this can result in reconstruction artifacts because for closer reflections, there are few pixels that could have contributed to the signal. However, for deeper reflections, there are many more pixels that could have caused the reflection, i.e. the deeper the reflection the less lateral resolution it has. Fig. 5 shows the back-projection of two point scatters of different depth. The closer reflection has less overlapping and higher lateral resolution. The deeper reflection has larger overlapping and lower lateral resolution. This is an issue because MBIR spreads the energy over the intersection area, which attenuates the intensity dramatically for deeper reflections. This smoothing and attenuation appear to increase more rapidly for deeper reflection. Therefore, a linear spatially-variant regularization as in [13] is not sufficient, and a more generalized model is needed. Hence, we adapt a non-linear spatially-variant regularization technique designed for the UNDE system. We can solve the attenuation problem by assigning less regularization as the pixel gets deeper. The disadvantage of this method is that it will amplify both the reflection and the noise for deeper pixels.

We replace σ_g and σ_e with $\sigma_{g_{s,r}}$ and σ_{e_s}, respectively, where these new parameters are monotone increasing with respect to depth. We assign a new scaling parameter c_s that varies between two values, 1 and c_{max}, as follows:

$$c_s = 1 + (c_{\text{max}} - 1) * \left(\frac{\text{depth of pixel } s}{\text{maximum depth}}\right)^a \tag{11}$$

where $a > 0$ and $c_{max} > 1$. Then, $\sigma_{g_{s,r}}$ and σ_{e_s} are calculated as follows:

$$\begin{aligned}
\sigma_{g_{s,r}} &= \sigma_g\sqrt{c_s c_r}, \\
\sigma_{e_s} &= \sigma_e c_s\ ,
\end{aligned}$$

where c_r has the same equation as in c_s, but for pixel r.

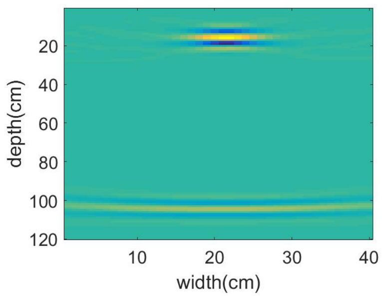

Fig. 5. Back-projection of two point scatters, one that is closer to the transducers (17cm deep) and one that is far from the transducers (105 cm deep). As the reflection gets deeper, The lateral resolution decreases.

B. Selection of Prior Model Parameters

The selection of the prior model parameters is an open area of research. In this paper, we select the regularization parameters σ_g, σ_e and γ (which control edge preservation, background sparsity, and contribution from neighbors of adjacent layers, respectively) to produce the best results visually. The parameters p, q, T, and a (which controls the transitioning from high to low regularization as the pixels get deeper) are unitless parameters and the values used for them in this paper are considered standard and seem to be consistent with the applications we are working on. The parameter c_{max} is a unitless parameter and is used to amplify reflections for deeper regions as needed.

IV. Optimization of MAP Cost Function

After designing the forward model and the prior model, the MAP estimate becomes

$$(x, g, \sigma^2)_{MAP} = \arg\min_{x\geq 0, g, \sigma^2} \left\{ \frac{1}{2\sigma^2} \|y - Ax - Dg\|^2 + \frac{MK}{2}\log(\sigma^2) + \sum_{\{s,r\}\in C} b_{s,r}\ \rho(x_s - x_r, \sigma_{g_{s,r}}) + \sum_{s\in S} \frac{x_s}{\sigma_{e_s}} \right\}. \tag{12}$$

The shifting of the direct arrival signal matrix D mentioned in section II-A is performed once before estimating g, x and σ^2. The solution for g is straightforward:

$$0 = \bigtriangledown_g \left\{ \frac{1}{2\sigma^2} \|y - Ax - Dg\|^2 + \frac{MK}{2}\log(\sigma^2) + \sum_{\{s,r\}\in C} b_{s,r}\ \rho(x_s - x_r, \sigma_{g_{s,r}}) + \sum_{s\in S} \frac{x_s}{\sigma_{e_s}} \right\}$$

$$\implies 0 = 2D^tDg + 2D^tAx - 2D^ty$$

$$\implies g = (D^tD)^{-1}D^t(y - Ax).$$

Given x, the evaluation of g is computationally inexpensive because D^tD is a diagonal matrix, i.e.

$$(D^tD) = \begin{bmatrix} d_1^td_1 & 0 & \dots & 0 \\ 0 & d_2^td_2 & \dots & 0 \\ \vdots & \vdots & \ddots & \vdots \\ 0 & 0 & \dots & d_K^td_K \end{bmatrix},$$

ICD Algorithm Using Majorization Technique

Initialize x, $e \leftarrow y - Ax$, σ^2

For $p = 1$: Number of transducer pairs{

$n_p = \arg\max_{n_p}\{y_p^t d_p(n - n_p)\}$

$d_p \leftarrow d_p(n - n_p)$

}

Repeat if stopping condition is not met {

$g = (d^td)^{-1}d^te$

$e \leftarrow e - dg$

For each pixel $s \in S${

$\tilde{b}_{s,r} \leftarrow \frac{b_{s,r}\rho'(x_s - s_r)}{2(x_s - x_r)}$

$\theta_1 \leftarrow -\frac{e^tA_{*,s}}{\sigma^2} + \sum_{r\in\partial s} 2\tilde{b}_{s,r}(x_s - x_r)$

$\theta_2 \leftarrow \frac{A_{*,s}^tA_{*,s}}{\sigma^2} + \sum_{r\in\partial s} 2\tilde{b}_{s,r}$

$\alpha^* \leftarrow \text{clip}\left\{\frac{-\theta_1}{\theta_2}, [-x_s, \infty)\right\}$

$e \leftarrow e - A_{*,s}\alpha^*$

$x_s \leftarrow x_s + \alpha^*$

}

$\sigma^2 \leftarrow \frac{\|e\|^2}{MK}$

}

Fig. 6. ICD algorithm using the majorization technique with shift error estimation (top red box) and direct arrival modeling (bottom red box) [30], [31].

where d_k is the discretized version of $\tilde{d}_k(t)$ for transducer pair k. However, g requires the knowledge of x which is the image we would like to reconstruct. This issue can be resolved by updating the value of g from the updated image in each iteration. Furthermore, for each iteration, we update g, x, and σ^2 in the following steps:

$$\begin{aligned} g &\leftarrow (D^tD)^{-1}D^t(y - Ax) \\ y &\leftarrow y - Dg \\ x &\leftarrow \arg\min_{x\geq 0}\left\{ -\log p(y|x) - \log p(x) \right\} \\ \sigma^2 &\leftarrow \frac{1}{MK}\|y - Ax\|^2 \end{aligned}$$

We adopt the iterative coordinate descent (ICD) technique to optimize the cost function with respect to x [31]. Since the prior model term is non-quadratic, optimizing the cost function will be computationally expensive. Therefore, we use the surrogate function (majorization) approach with ICD to resolve this issue [30]. This ICD optimization algorithm is guaranteed to converge to the global minimum because the function being minimized is continuously differentiable and strictly convex [30]. Fig. 6 shows the complete algorithm for ICD using the majorization approach. The algorithm is stopped either if

$$\frac{\|x_{n-1} - x_n\|}{\|x_{n-1}\|} < \epsilon, \tag{13}$$

where x_n is the current image update and ϵ is a stopping threshold, or if the number of iterations exceeds a specified number, e.g. 100 iterations. Empirically, we have found that a value of $\epsilon = 0.01$ is a sufficient value to declare convergence with zero initialization.

V. Results

In this section we compare MBIR with two different techniques qualitatively and quantitatively.

A. Algorithms for Comparison

We compare MBIR with the SAFT and l_1-norm techniques. The l_1-norm is a regularized iterative technique with the same forward model as in Eq. 5 with an exponential distribution prior. The prior model is exactly equal to an l_1 regularization term with a positivity constraint. The MAP estimate for the l_1-norm technique is

$$(x, \sigma^2)_{MAP} = \underset{x \geq 0, \sigma^2}{\arg\min} \left\{ \frac{1}{2\sigma^2} \|y - Ax\|^2 + \frac{MK}{2} \log(\sigma^2) + \sum_{s \in S} \frac{x_s}{\sigma_{e_s}} \right\}. \tag{14}$$

A pixel-wise precision-recall (PR) plot is used for the simulated data to compare the performance of the techniques qualitatively. A pixel-wise PR test calculates the number of true positive (TP), false positive (FP), and false negative (FN) for each technique. These values are, then, used to plot the precision vs. recall (PR) curves where

$$recall = \frac{TP}{TP + FN}$$

and

$$precision = \frac{TP}{TP + FP}.$$

This detection test compares the performance of each technique by the area under the PR curve. The larger the area the better the technique. Next, for each technique, all the images are normalized by dividing them with their maximum value. Thresholds from 1 to 0 with step 0.001 are applied to all images. For each threshold, a TP is declared if the defect diagram (ground truth) pixel is 1 and the reconstructed pixel is 1. A FP is declared if the defect diagram pixel is 0 and the reconstructed pixel is 1. A FN is declared if the defect diagram pixel is 1 and the reconstructed pixel is 0.

The techniques performance for the simulated data will be compared with measurements of different signal-to-noise ratio (SNR). The SNR is defined as

$$SNR = \frac{\|y\|^2}{\|w\|^2},$$

where y is the noiseless simulated output from k-wave, and w is the added noise to y.

A component-wise PR plot is used for the experimental data to compare the performance of each technique. Each image is segmented into connected components using the standard Matlab functions “edge” and “imfill”. Next, the maximum value and weighted centroid for each connected component is stored. Next, a search is performed pairing targets from the defect diagram to connected components from the reconstruction in the following way: A connected component is mapped to a particular target if its centroid is both the closest among all detected components to the target’s centroid, and it is within 10 cm of the target’s centroid. Next, for each technique, all the images are normalized by dividing them with the maximum value of them all. Thresholds from 1 to 0 with step 0.001 are applied to all images. For each threshold, a TP is declared if the maximum value of a paired connected component is equal or greater than the threshold. A FP is declared if the maximum value of an unpaired connected component is equal or greater than the threshold. The FN is calculated by subtracting the number of TP’s from the number of targets.

A normalized root mean square error (NRMSE) plot will be used to compare MBIR convergence with different initializations. The NRMSE is defined as

$$NRMSE(n) = \frac{\|X_n - X_{true}\|}{\|X_{true}\|}, \tag{15}$$

where n is the iteration number, and X_{true} is the true solution. We define X_{true} to be iteration 1500 of the zero initialization.

B. K-wave Simulated Results

The k-wave simulator have been used to simulate acoustic propagation through concrete medium [32]. The concrete structure was embedded with steel of different shapes. The width and depth of the structure is 40cm and 30cm , respectively. 10 transducers were used to transmit and receive. For each simulation, the simulator produces 90 outputs from all pairs of transducers where only distinctive pairs are used, i.e. 45 distinctive pairs. The transducers are placed at the top center of the field-of-view and separated by 4cm from each other. To simulate the acoustic propagation using k-wave, we provided three images of speed, density, and attenuation as inputs to k-wave. Each pixel in the three input images corresponds to the characteristics of either steel or cement. The output of k-wave is then used as input to the reconstruction methods. Fig. 7 shows reconstruction results for four different tests. The voxel spacing for 2D reconstructions is 1 cm for all reconstruction techniques. The left column shows the designed defect diagram that was used for simulation where the white pixels corresponds to cement and the black pixels corresponds to steel. The next column shows the instantaneous envelope of SAFT reconstruction. The next column is l_1-norm. The right column shows the MBIR reconstruction. Both l_1-norm and MBIR were initialized to zero. Note that SAFT does not share the same unit with MBIR or L1-norm. That is why it shows different scaling.

Fig. 9 shows the pixel-wise PR curve for each technique over all 4 tests. Table IV shows values of the area under the PR curves in Fig. 9. Table I shows the parameters which are used for k-wave simulation, and some of them are used as input parameters in all techniques. Table III shows the parameters used for l_1-norm and MBIR in Eq. 1, 9, and 11, and the stopping threshold.

Fig. 8 shows a comparison between the methods with noise added to the simulated signal of the defect diagram of Test 1 in Fig. 7.

Discussion: In Fig 7, MBIR and l_1-norm were able to show significant enhancement over SAFT in reducing noise. MBIR showed remarkable performance in identifying, eliminating, and distinguishing the direct arrival signal artifacts from the steel objects. For example, in test 1, two steel plates where placed at depth 2cm. The plates where overshadowed by the direct arrival signal artifacts in SAFT and l_1-norm, but appear

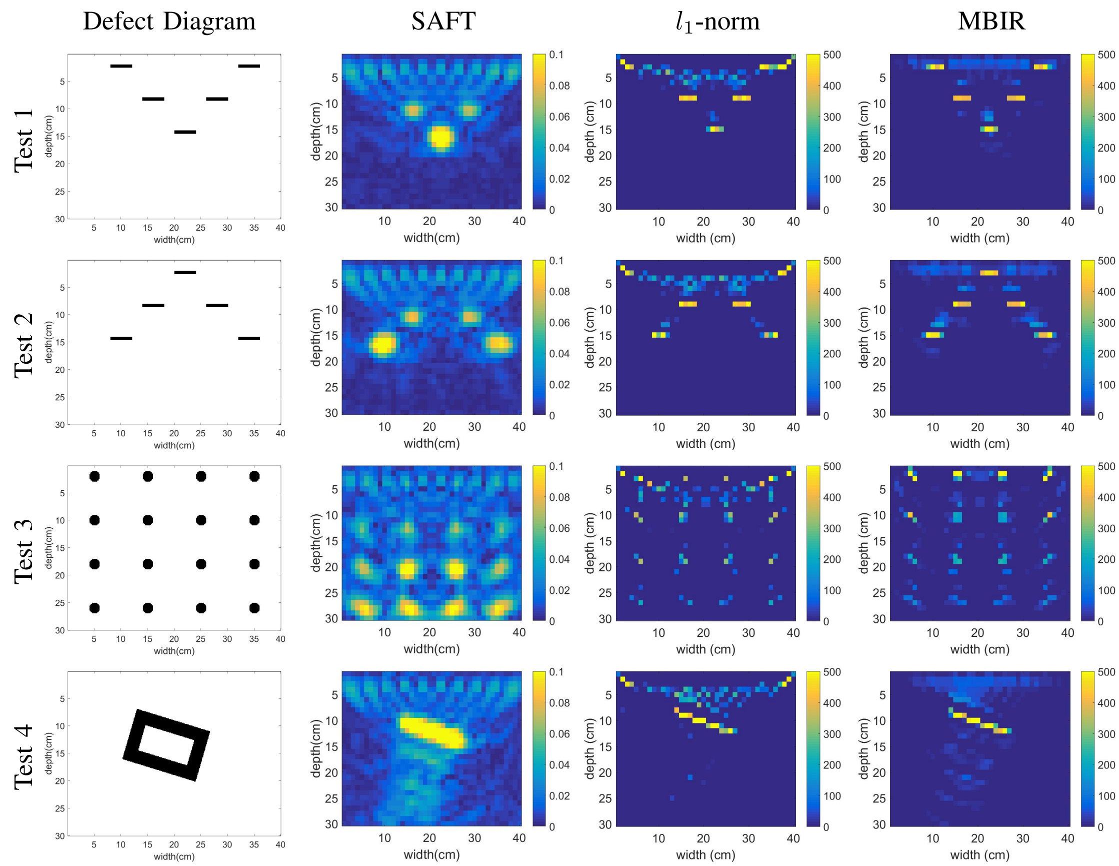

Fig. 7. Comparison between MBIR and SAFT reconstruction from the k-wave simulated data. The far left column is the position of the defects. The next column is SAFT reconstruction. The next column is l_1-norm reconstruction. The far right column is MBIR reconstruction. MBIR tends to produce results with less noise and artifacts compared to SAFT and l_1-norm.

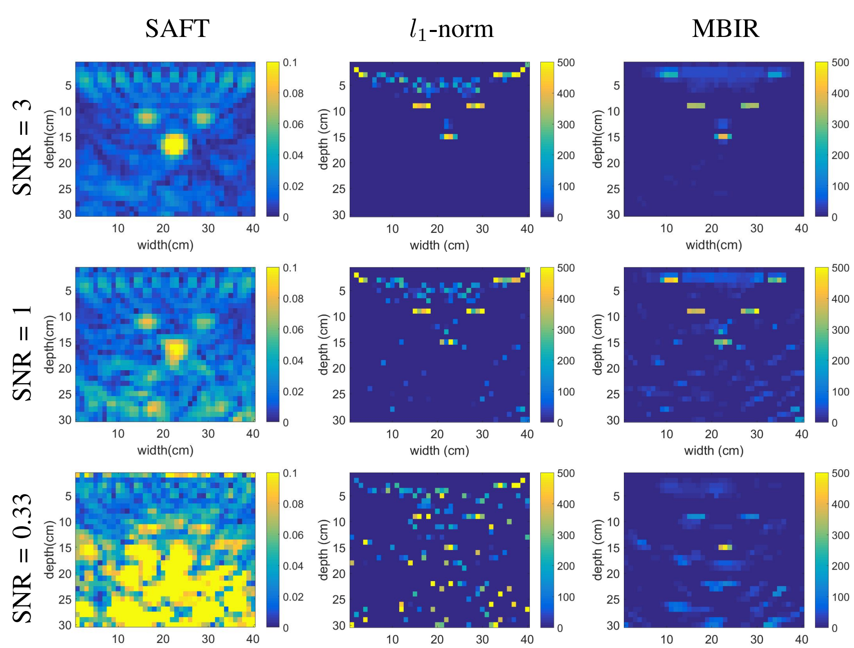

Fig. 8. Comparison between SAFT, l_1-norm, MBIR reconstructions from the k-wave simulated data with different SNR. The defect diagram is the same as the defect diagram in Test 1 in Fig. 7. The left column is SAFT reconstruction. The next column is l_1-norm reconstruction. The right column is MBIR reconstruction. Each row correspond to different SNR value where the SNR values from top to bottom are 3, 1, and 0.33, repectively. MBIR tends to produce results with less noise and artifacts compared to SAFT and l_1-norm.

TABLE I
PARAMETER SETTINGS FOR K-WAVE SIMULATION.

Parameters	Value	Unit
Carrier frequency	52	kHz
Sampling frequency	1	MHz
Cement speed	3680	m/s
Cement density	1970	Kg/m^3
Cement attenuation	1.46e-6	$dB/((MHz)^y cm)$
Steel speed	5660	m/s
Steel density	8027	Kg/m^3
Steel attenuation	4.85e-8	$dB/((MHz)^y cm)$
Spatial resolution	1	mm
Number of columns	400	-
Number of rows	300	-
Number of transducers	10	-

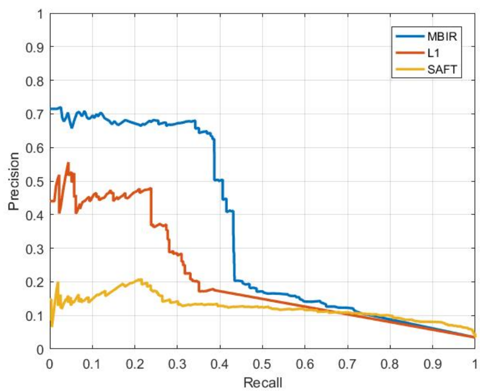

Fig. 9. PR curves for each technique over all 4 tests in Fig.7. MBIR outperforms the other techniques by having the highest PR area.

very clearly in MBIR. Test 2 and 3 also show similar direct arrival signal overshadowing effects for SAFT and l_1-norm, that are reduced for MBIR. In addition, the steel objects are more easily observed and recognized in l_1-norm and MBIR. In Fig. 9 and Table IV, MBIR shows better performance in the detection test with the highest PR area.

Notice that in test 4, none of the techniques were able to show the complete structure of the steel object. They were able to show only one side of it. This is because all three reconstruction methods reconstruct the reflections caused by discontinuous boundaries rather than recovering the actual material property at each voxel location.

Fig. 8 shows the reconstruction of test 1 in Fig. 7 with varying signal-to-noise ratio (SNR). As the SNR decreases, the reconstruction becomes noisier for all techniques. However, the results show better performance in MBIR than the other techniques in reducing noise and artifacts.

C. MIRA Experimental Results

Experimental results have been obtained from a designed thick concrete specimen [33]. The height and width of the specimen is 213.36 cm (84 inches), Fig. 10. The depth of the specimen is 101.6 cm (40 inches). Each side of the block is gridded with 10.16 cm squares producing 21 rows and columns. The specimen has been heavily reinforced with steel rebars horizontally and vertically with 1 ft separation in both sides. One side is "smooth" and the other is "rough" which refer to the physical characteristic of the concrete surface due to pouring. Also, Fig. 12 and Fig. 13 show diagrams of the steel rebars in green color with more details. The specimen has been embedded with designed defects placed in specific locations. The type and location of the defects are shown in Figs. 11, 12, 13, and 14 [33]. The specified location of the defects might be different from the real location due to possible displacement while pouring the cement.

The defects are designed to simulate real defects that can occur due to construction process, cumulative deterioration, or degradation of concrete. Both sides are scanned horizontally and vertically. There are four types of scanning modes: smooth-horizontal (SH), smooth-vertical (SV), rough-horizontal (RH), and rough-vertical (RV). Each mode divides the whole side into 19 sets which adds up to 76 sets. However, only 73 sets are used and are arranged in this order: sets 1 to 18 for SH, sets 19 to 37 for SV, sets 38 to 56 for RH, and sets 57 to 73 for RV. Each set scans the side from left to right or from bottom to top, depending on the orientation of the mode, with 18 positions. The first and last positions are centered at 20.32 cm (8 inches) from the edge. The rest of the positions are centered with a 10.16-cm (4-inch) shift from the previous position, hence the 18 positions.

The MIRA system has been used to collect the data, Fig. 15. The MIRA device contains 10 columns or channels separated by 40 mm where each channel contains 4 dry contact points with 2 mm radius that acts as transmitters or receivers. Only distinct pairs, 45 pairs, are used in the reconstruction results for all techniques. Each position produces an image of width 40 cm and depth 120 cm with 1 cm resolution. SAFT requires approximately 0.03 seconds to reconstruct an individual image, and MBIR requires approximately 5 seconds for the same image. There are four different techniques used to reconstruct the data: SAFT, l_1-norm, 2D MBIR, and 2.5D MBIR. Zero initialization was used for l_1-norm, 2D MBIR, and 2.5D MBIR. For SAFT, the multiple scans are jointly reconstructed to avoid the stitching artifacts. For l_1-norm, all images of the set are stitched together to produce the complete cross section of the set with 210cm-width and 120cm-depth. For 2D MBIR, and 2.5D MBIR, the joint-MAP stitching is used to reconstruct the whole cross section at once instead of regular stitching. The joint-MAP stitching reduced the MBIR processing time of the whole data from about 110 minutes to about 87 minutes (about 30% lower). However, the 2.5D MBIR increased the processing time from 87 minutes to 126 minutes (about 45% higher). All the techniques were implemented in Windows with a 6th generation Intel core i7-6500U processor with 4 MB cache, 2/4 core/threads, and 2.5 GHz CPU. The transmitter emits a signal with carrier frequency of 52 kHz, and the sampling frequency of the receiver is 1 MHz. The acoustic speed is assumed to be $2620\frac{m}{s}$. Each distinct pair produces 2048 samples of data where the first 27 samples are ignored due to trigger synchronization. The data is, then, down-sampled to 200 kHz and 409 samples and reconstructed using all techniques.

Fig. 16 shows the reconstruction results. The reconstruction 2D voxel spacing is 1 cm for all techniques. The rows are

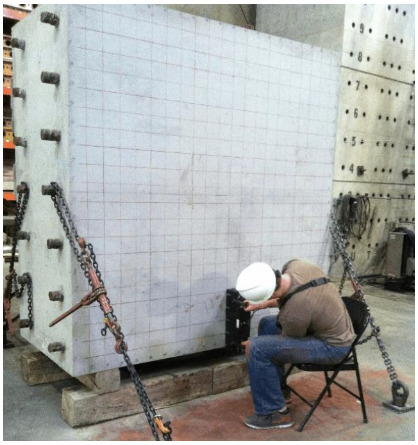

Fig. 10. The concrete specimen used for the experimental data [33]. 20 defects are embedded in the specimen.

ordered from top to bottom. The first row shows the defect diagram and the position of the defects. The scanning of the cross sections was performed at the top of the image from left to right. The second row is the instantaneous envelope of SAFT reconstruction. The third row is l_1-norm reconstruction. The fourth row is 2D MBIR reconstruction. The fifth row is 2.5D MBIR reconstruction. Note that the defect diagram shows the steel rebars as dotted circles or dotted rectangles. The steel rebars might appear in all reconstructions as small horizontal dots or a horizontal line at the top, but the bottom steel rebars barely appear in all techniques due to their weak reflection. Table II shows the common parameter settings for all techniques. Table III shows the l_1-norm and MBIR parameter settings for Eq. 1, 9, and 11, γ in section III, and the stopping threshold.

Because the position of the targets in the defect diagram is not precise, the detection test was done using a component wise approach rather than the pixel-wise approach used for the k-wave data. Fig. 17 shows the PR curve for each technique over all 73 experimental data sets. To make a fair comparison, the parameter σ_g for MBIR, the parameter σ_e for l_1-norm, and the parameters σ_g and γ for 2.5D MBIR were chosen using a grid search to maximize the area under the PR curves. Table IV shows the value of the area under the PR curves in Fig. 17.

Discussion: In Fig. 16, MBIR shows significant enhancement in reducing artifacts and reducing noise compared with SAFT and l_1-norm. SAFT and MBIR techniques were able to show the back wall of the specimen. The back wall is located at depth 100 cm. The detection test showed better performance of 2.5D and 2D MBIR over all techniques with 2.5D MBIR being slightly better than 2D MBIR.

Since all three algorithms are based on a linear forward model, they all exhibit certain reconstruction artifacts such as multiple reflection echos of a single defect. For example, multiple echos appeared of defect 13 in SV8 for all techniques.

DEFECT TABLE		
ID NUMBER	DESCRIPTION	LABEL
D1	POROUS HALF CYLINDER (NO COVER)	
D2	POROUS HALF CYLINDER (COVER)	
D3	POROUS HALF CYLINDER (NO COVER)	
D4	POROUS HALF CYLINDER (COVER)	
D5	POROUS HALF CYLINDER (COVER & CRACK)	
D6	PVC	
D7	PVC	
D8	DISSOLVING STYROFOAM (THICK)	
D9	STYROFOAM (THICK)	
D10	STYROFOAM (THIN)	
D11	PLEXIGLASS	
D12	DISSOLVING STYROFOAM (MEDIUM)	
D13	STYROFOAM (MEDIUM)	
D14	PLEXIGLASS	
D15	DISSOLVING STYROFOAM (THIN)	
D16	LUMBER (2X4)	
D17	GLOVES	
D18	DEBOND DUCT TAPE (ONE LAYER)	
D19	DEBOND DUCT TAPE (MULTI–LAYER)	
D20	MOVING REBAR	

Fig. 11. Type and legend for each defect [33]. These defects are embedded in the concrete specimen.

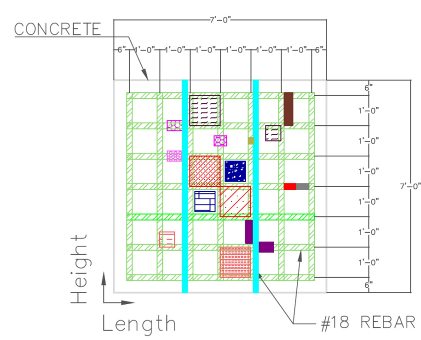

Fig. 12. Smooth side view of defects [33]. The location of the defects is approximated due to possible displacement while pouring the cement.

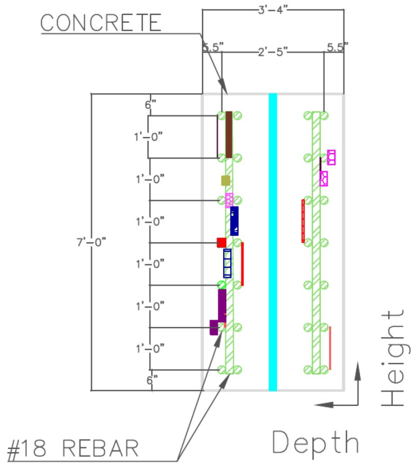

Fig. 13. Depth view of defects, smooth side on the right and rough side on the left, [33]. The location of the defects is approximated due to possible displacement while pouring the cement.

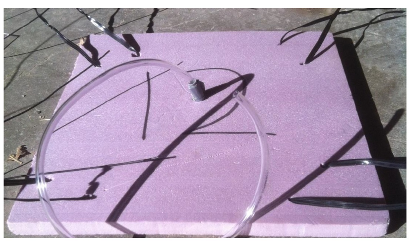

Fig. 14. A picture of defect 12 before embedding it in the specimen, [33]. It is made of dissolving styrofoam.

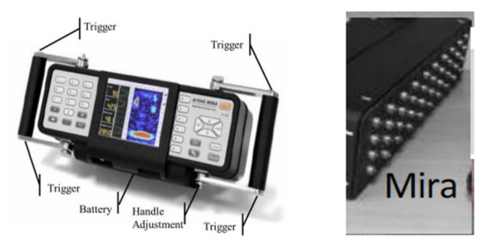

Fig. 15. A picture of the MIRA device used for the experimental data. The device has 10 columns of transducers, where each column acts as a single transducer.

TABLE II
PARAMETER SETTINGS USED FOR ALL TECHNIQUES TO RECONSTRUCT THE EXPERIMENTAL MIRA DATA.

Parameters	Value	Unit
Carrier frequency	52	kHz
Sampling frequency	200	kHz
Cement p-wave speed	2620	m/s
Reconstruction resolution	1	cm
Number of columns	210	-
Number of rows	120	-

D. Results from Modifying the Forward and Prior Models

In this section, we investigate the effect of various MBIR model attributes on the image quality resulting from the MIRA data reconstructions. In particular, we computed reconstructions *without* direct arrival signal elimination, shift error estimation, anisotropic reconstruction, and spatially variant regularization. We then compared each of these degraded results to the baseline MBIR reconstructions using the complete MBIR algorithm in order to better understand the value of each technique in overall image quality. We also calculated the component-wise PR area for each reconstruction.

Fig. 18 compares MBIR performance when not using each modification. Fig. 18b shows 2D MBIR reconstruction with PR area = 0.5906. Fig. 18c shows 2.5D MBIR reconstruction with PR area = 0.6199. Fig. 18d shows 2D MBIR reconstruction without the direct arrival signal modeling with PR area = 0.4235. Fig. 18e shows 2D MBIR reconstruction with the direct arrival signal modeling, but not the shift error estimation, with PR area = 0.4827. Fig. 18f shows 2D MBIR reconstruction with regular stitching with PR area = 0.4384. Fig. 18g shows 2D MBIR reconstruction with an isotropic forward model with PR area = 0.4951. Fig. 18h shows 2D MBIR reconstruction with constant regularization with PR area = 0.5234. All the PR areas specified in Fig. 18 were obtained by calculating the precision and recall for each plot for only the cross-section shown in Fig. 18a.

Discussion: Fig. 18d does not model the direct arrival which causes the reconstruction to have artifacts at the top of the image. These artifacts have high amplitude and could overshadow targets closer to the transducers. Fig. 18e reduces these artifacts by modeling the direct arrival signal. However, some residual of the artifacts still appears at the top right corner due to changes in acoustic speed in the concrete medium. Fig. 18f shows the results of performing conventional stitching technique to stitch the reconstruction from multiple scans. The stitching method produces vertical discontinuities at the boundaries between the stitched images. Also, the stitching method does not make use of additional information that can be obtained from adjacent scans to improve the reconstruction. Fig. 18g uses an isotropic model for the transmitted beam which produces artifacts at the top of the image. These artifacts appear because of the assumption that the signal travels in all directions equally which allows MBIR to use pixels with large transmitter-pixel or pixel-receiver angles to fit the data. Fig. 18h uses a spatially constant regularization which suppresses weak details in deep regions of the reconstruction. This results from the fact that the signal is dramatically attenuated as it propagates into deeper regions. Consequently, reconstruction with a constant regularization attenuates most useful detail in the deep parts of the image.

In contrast, Fig. 18b shows 2D MBIR with much better performance in reducing artifacts, exploiting correlations from adjacent scans, showing targets for deeper regions, and having larger PR area. Finally, Fig. 18c shows the 2.5D MBIR reconstruction which is qualitatively and quantitatively slightly better than 2D MBIR.

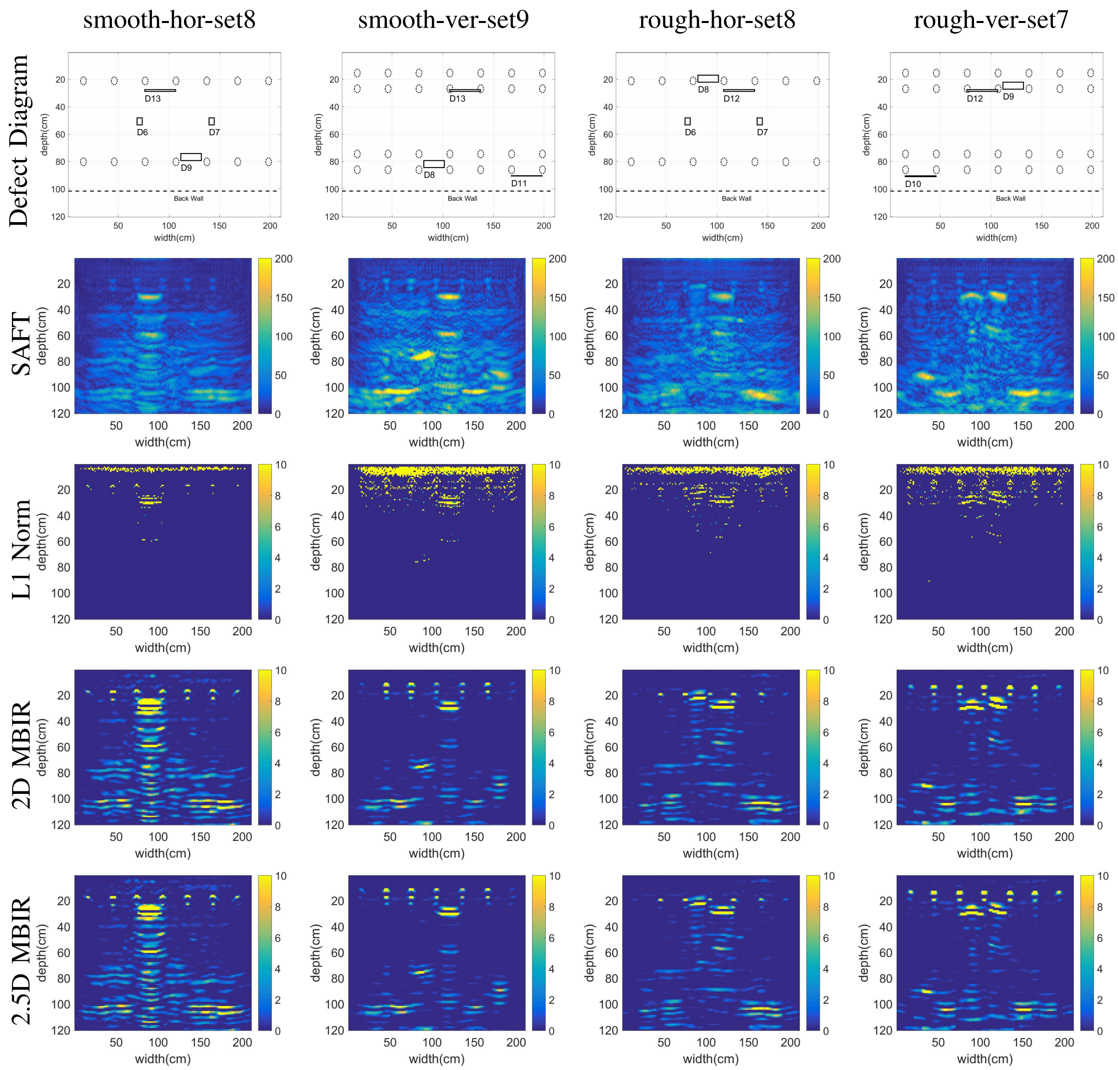

Fig. 16. Comparison between all reconstruction results from the MIRA experimental data: the first row from the top is the position of the defects, the second row is SAFT reconstruction, the third row is l_1-norm reconstruction, the fourth row is 2D MBIR reconstruction, and the fifth row is 2.5D MBIR reconstruction. 2.5D and 2D MBIR tend to produce results with less noise and artifacts compared to other techniques.

TABLE III
THE l_1-NORM, 2D MBIR, AND 2.5D MBIR PARAMETER SETTINGS USED IN THE SIMULATED K-WAVE AND THE EXPERIMENTAL MIRA DATA.

Parameters	**l_1-norm**	**2D MBIR**	**2.5D MBIR**	**Unit**
ϵ	0.01	0.01	0.01	-
α_0	30	30	30	$(MHz \cdot m)^{-1}$
p	-	1.1	1.1	-
q	-	2	2	-
T	-	1	1	-
c_{max}	-	10	10	-
a	-	3	3	-
σ_g	-	3	3	m^{-3}
σ_e	15	15	15	m^{-3}
γ	-	-	0.5	-

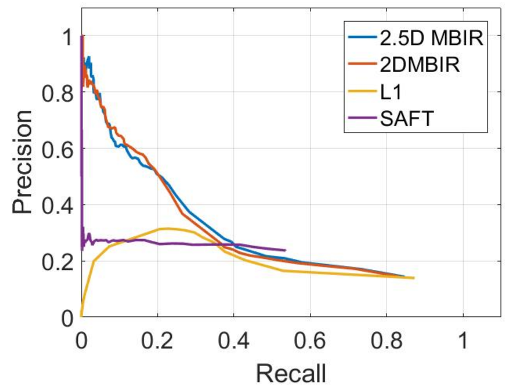

Fig. 17. PR curves for each technique over all 73 experimental data sets. 2.5D and 2D MBIR outperforms the other techniques.

TABLE IV
PRECISION VS RECALL AREA FOR ALL TECHNIQUES IN FIG. 9 AND FIG. 17. MBIR HAS THE HIGHEST PR AREA.

	SAFT	l_1-norm	2D MBIR	2.5D MBIR
PR area for k-wave data	0.1236	0.2131	0.3476	-
PR area for MIRA data	0.1397	0.1932	0.2836	0.2908

E. Convergence of MBIR

To show the algorithm's convergence behavior, we reconstructed cross-section rough-hor-set11 in Fig. 18a from the MIRA data with different initializations: uniformly distributed random noise with range [0, 10], zero, a constant value of 10. Fig. 19 shows the NRMSE vs. iteration for the different initializations.

VI. CONCLUSION

This paper proposed an MBIR algorithm for ultrasonic one-sided NDE. The paper showed the derivation of a linear forward model. The QGGMRF potential function for the Gibbs distribution prior model was chosen for this problem because it guarantees function convexity, models edges and low contrast regions, and has continuous first and second derivatives. Furthermore, we proposed modifications to both the forward and prior models that improved reconstruction quality. These modifications included direct arrival signal elimination, anisotropic transmit and receive pattern, and spatially variant regularization. Additionally, a joint-MAP estimate and a 2.5D MBIR were performed to process large multiple scans at once which helps reduce noise and artifacts dramatically compared with results from individual scans. The research was supported by simulated and extensive experimental results. The results compared the performance of MBIR with SAFT and l_1-norm qualitatively and quantitatively. The results showed noticeable improvements in MBIR over SAFT and l_1-norm in reducing noise and artifacts.

While the results of this paper are promising, it is worth mentioning the need of a non-linear forward model to address the issues due to the complexity of the one-sided UNDE systems, such as reverberation, and acoustic shadowing.

VII. ACKNOWLEDGMENT

Hani Almansouri and C.A. Bouman were supported by the U.S. Department of Energy. S.Venkatakrishnan and Hector Santos-Villalobos were supported by the U.S. Department of Energy's staff office of the Under Secretary for Science and Energy under the Subsurface Technology and Engineering Research, Development, and Demonstration (SubTER) Crosscut program, and the office of Nuclear Energy under the Light Water Reactor Sustainability (LWRS) program.

REFERENCES

[1] P. Ramuhalli, J. W. Griffin, R. M. Meyer, S. G. Pitman, J. M. Fricke, M. E. Dahl, M. S. Prowant, T. A. Kafentzis, J. B. Coble, and T. J. Roosendaal, *Nondestructive Examination (NDE) Detection and Characterization of Degradation Precursors, Technical Progress Report for FY 2012*. Washington, D.C. : United States. Office of the Assistant Secretary for Nuclear Energy ; Oak Ridge, Tenn. : distributed by the Office of Scientific and Technical Information, U.S. Dept. of Energy, 2012.

[2] M. Berndt, "Non-destructive testing methods for geothermal piping." 2001.

[3] J. Zemanek, E. E. Glenn, L. J. Norton, and R. L. Caldwell, "Formation evaluation by inspection with the borehole televiewer," *Geophysics*, vol. 35, no. 2, pp. 254–269, 1970.

[4] K. Hoegh and L. Khazanovich, "Extended synthetic aperture focusing technique for ultrasonic imaging of concrete," *NDT and E International*, vol. 74, p. 33–42, 2015.

[5] T. Stepinski, "An implementation of synthetic aperture focusing technique in frequency domain," *ieee transactions on ultrasonics, ferroelectrics, and frequency control*, vol. 54, no. 7, 2007.

[6] M. Li and G. Hayward, "Ultrasound Nondestructive Evaluation (NDE) imaging with transducer arrays and adaptive processing," *Sensors*, vol. 12, no. 12, p. 42–54, 2011.

[7] J. Haldorsen, D. Johnson, T. Plona, B. Sinha, H. Valero, and K. Winkler, "Borehole acoustic waves," *Oilfield Review*, vol. 18, no. 1, pp. 34–43, 2006.

[8] Z. Shao, L. Shi, Z. Shao, and J. Cai, "Design and application of a small size SAFT imaging system for concrete structure," *Review of Scientific Instruments*, vol. 82, no. 7, p. 073708, 2011.

[9] B. J. Engle, J. L. W. Schmerr, and A. Sedov, "Quantitative ultrasonic phased array imaging," *AIP Conf. Proc.*, vol. 1581, no. 7, p. 49, 2014.

[10] G. Dobie, S. G. Pierce, and G. Hayward, "The feasibility of synthetic aperture guided wave imaging to a mobile sensor platform," *NDT and E International*, vol. 58, no. 7, pp. 10–17, 2013.

[11] S. Beniwal and A. Ganguli, "Defect detection around rebars in concrete using focused ultrasound and reverse time migration," *Ultrasonics*, vol. 62, p. 112–125, 2015.

[12] M. Schickert, M. Krause, and W. Müller, "Ultrasonic imaging of concrete elements using reconstruction by synthetic aperture focusing technique," *Journal of Materials in Civil Engineering*, vol. 15, no. 3, pp. 235–246, 2003.

[13] E. Ozkan, V. Vishnevsky, and O. Goksel, "Inverse problem of ultrasound beamforming with sparsity constraints and regularization," *IEEE transactions on ultrasonics, ferroelectrics, and frequency control*, vol. 65, no. 3, pp. 356–365, 2018.

[14] H. Wu, J. Chen, S. Wu, H. Jin, and K. Yang, "A model-based regularized inverse method for ultrasonic B-scan image reconstruction," *Measurement Science and Technology*, vol. 26, no. 10, p. 105401, 2015.

[15] A. Tuysuzoglu, J. M. Kracht, R. O. Cleveland, M. Çetin, and W. C. Karl, "Sparsity driven ultrasound imaging a," *The Journal of the Acoustical Society of America*, vol. 131, no. 2, pp. 1271–1281, 2012.

[16] G. A. Guarneri, D. R. Pipa, F. N. Junior, L. V. R. de Arruda, and M. V. W. Zibetti, "A sparse reconstruction algorithm for ultrasonic images in nondestructive testing," *Sensors*, vol. 15, no. 4, pp. 9324–9343, 2015.

[17] T. Szasz, A. Basarab, and D. Kouamé, "Beamforming through regularized inverse problems in ultrasound medical imaging," *IEEE transactions on ultrasonics, ferroelectrics, and frequency control*, vol. 63, no. 12, pp. 2031–2044, 2016.

[18] H. M. Shieh, H.-C. Yu, Y.-C. Hsu, and R. Yu, "Resolution enhancement of nondestructive testing from b-scans," *International Journal of Imaging Systems and Technology*, vol. 22, no. 3, pp. 185–193, 2012.

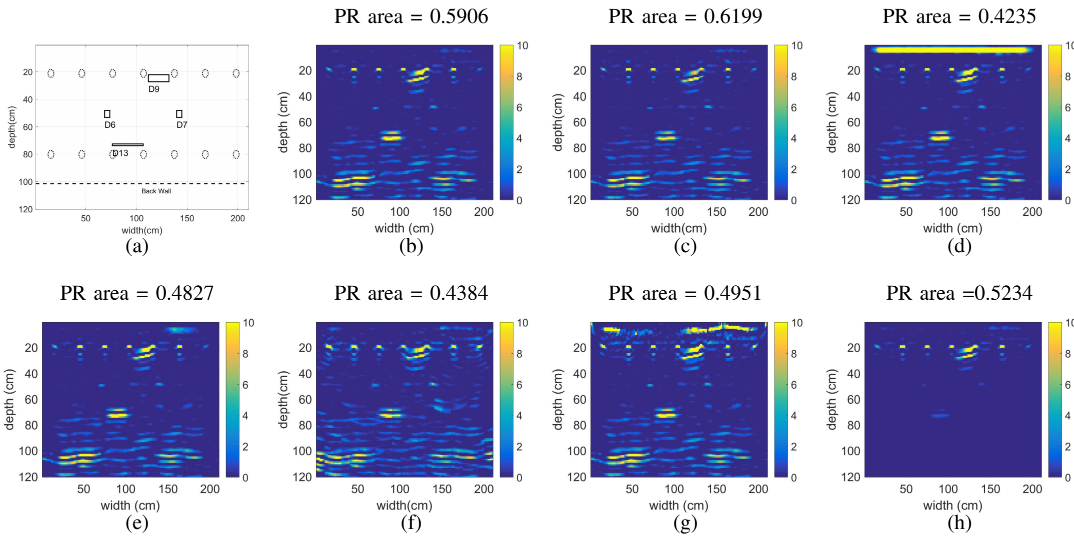

Fig. 18. A comparison between different settings of MBIR where (a) is the defect diagram of rough-hor-set11, (b) is 2D MBIR reconstruction, (c) is 2.5D MBIR reconstruction with all modifications to the forward and prior models, (d) is 2D MBIR reconstruction without direct arrival signal or shift error estimation, (e) is 2D MBIR reconstruction without shift error estimation, (f) is 2D MBIR reconstruction using regular stitching, (g) is 2D MBIR reconstruction using an isotropic model, (h) is 2D MBIR reconstruction for a constant regularization. The results in (c) shows performance enhancement over the other results.

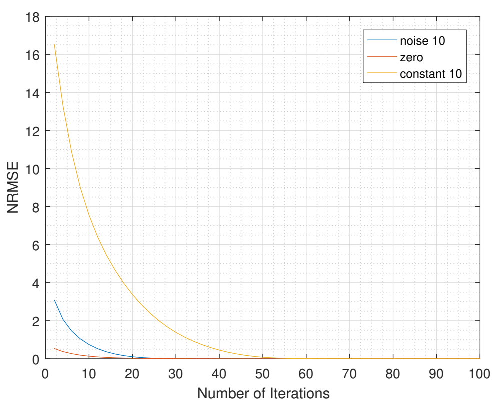

Fig. 19. NRMSE vs. iteration for different initializations in the MBIR algorithm. The initializations used in the plot are uniformly distributed random noise with range [0, 10], zero, and a constant value of 10, respectively.

[19] H. Almansouri, C. Johnson, D. Clayton, Y. Polsky, C. Bouman, and H. Santos-Villalobos, "Progress implementing a model-based iterative reconstruction algorithm for ultrasound imaging of thick concrete," in *AIP Conference Proceedings*, vol. 1806, no. 1. AIP Publishing, 2017, p. 020016.

[20] H. Almansouri, S. Venkatakrishnan, D. Clayton, Y. Polsky, C. Bouman, and H. Santos-Villalobos, "Anisotropic modeling and joint-map stitching for improved ultrasound model-based iterative reconstruction of large and thick specimens," in *AIP Conference Proceedings*, vol. 1949, no. 1. AIP Publishing, 2018, p. 030002.

[21] ——, "Ultrasonic model-based iterative reconstruction with spatially variant regularization for one-sided non-destructive evaluation," *Electronic Imaging*, vol. 2018, no. 15, pp. 103–1, 2018.

[22] A. Kak and K. A. Dines, "Signal processing of broadband pulsed ultrasound: Measurement of attenuation of soft biological tissues," *IEEE Transactions on Biomedical Engineering*, vol. BME-25, no. 4, pp. 321–344, 1978.

[23] S. J. Norton and M. Linzer, "Ultrasonic reflectivity imaging in three dimensions: Exact inverse scattering solutions for plane, cylindrical, and spherical apertures," *IEEE Transactions on Biomedical Engineering*, vol. BME-28, no. 2, pp. 202–220, 1981.

[24] J. W. Wiskin, "Inverse scattering from arbitrary two-dimensional objects in stratified environments via a Green's operator," *The Journal of the Acoustical Society of America*, vol. 102, no. 2, p. 853, 1997.

[25] T. Huttunen, M. Malinen, J. Kaipio, P. White, and K. Hynynen, "A full-wave Helmholtz model for continuous-wave ultrasound transmission," *IEEE Transactions on Ultrasonics, Ferroelectrics and Frequency Control*, vol. 52, no. 3, p. 397–409, 2005.

[26] T. Voigt, *The application of an ultrasonic shear wave reflection method for nondestructive testing of cement-based materials at early ages: an experimental and numerical analysis*. Books on Demand, 2005.

[27] B. E. Treeby and B. T. Cox, "Fast tissue-realistic models of photoacoustic wave propagation for homogeneous attenuating media," *Photons Plus Ultrasound: Imaging and Sensing 2009*, Dec 2009.

[28] B. E. Treeby, M. Tumen, and B. T. Cox, "Time Domain Simulation of Harmonic Ultrasound Images and Beam Patterns in 3D Using the k-space Pseudospectral Method," *Lecture Notes in Computer Science Medical Image Computing and Computer-Assisted Intervention – MICCAI 2011*, p. 363–370, 2011.

[29] M. Li and G. Hayward, "Ultrasound nondestructive evaluation (nde) imaging with transducer arrays and adaptive processing," *Sensors*, vol. 12, no. 1, pp. 42–54, 2011.

[30] C. Bouman, *Model Based Image Processing*, 1st ed. Purdue University, 2013.

[31] Z. Yu, J.-B. Thibault, C. A. Bouman, K. D. Sauer, and J. Hsieh, "Fast model-based x-ray ct reconstruction using spatially nonhomogeneous icd optimization," *IEEE Transactions on image processing*, vol. 20, no. 1, pp. 161–175, 2011.

[32] B. E. Treeby and B. T. Cox, "k-Wave: MATLAB toolbox for the simulation and reconstruction of photoacoustic wave fields," *Journal of biomedical optics*, vol. 15, no. 2, pp. 021 314–021 314, 2010.

[33] D. A. Clayton, A. M. Barker, H. J. Santos-Villalobos, A. P. Albright, K. Hoegh, and L. Khazanovich, "Nondestructive evaluation of thick concrete using advanced signal processing techniques," Jan 2015.